The Retarding Bessel-Box –
An Electron-Spectrometer designed for Pump/Probe Experiments

G. Schiwietz[1G], M. Beye[1], D.Kühn[1], and G. Xiao[1,2]

[1]Institute G-ISRR and also former Division HMI/SF8, Helmholtz-Zentrum Berlin f. Materialien u. Energie, Hahn-Meitner-Platz 1, 14109 Berlin, Germany
[2]Institute of Modern Physics, P.O. Box 31, Lanzhou 730000, P.R. China

Abstract

A new type of electrostatic electron spectrometer is developed, capable of particular sensitive measurements of energy spectra and time-of-flight distributions. This instrument is specifically designed and optimized for laser-pump/x-ray-probe measurements, where photo electrons or Auger electrons from surfaces, clusters, molecular or atomic targets are being measured with high time-resolution at an extremely low detection-noise level. The compact and robust cylinder-symmetrical system is a strongly improved Bessel-box design, featuring electron retardation, a large detection solid-angle, about 100% electron transmission (gridless design) and excellent time-resolution. In this paper we describe the principle of operation of this type of spectrometer and various tests. We present quantitative results for electron measurements with different solid-state targets and two different electron-detection systems in comparison to electron-trajectory simulations inside the electrostatic spectrometer fields. Picosecond-pump/probe operation has been tested with high laser power and even the ability to work under femtosecond-pump-probe conditions with electron detection at the BESSY II slicing facility has been proven.

PACS numbers: *79.20.Rf, 71.20.Ps, 31.70.Hq, 32.80.Hd, 61.80.Jh*

Keywords: *Electron Spectrometer, Detection-Solid-Angle, Transmission, Energy Resolution, Electron Emission, Femtosecond-Pump/Probe Experiments, Short-time Electron Dynamics, Surface Physics, Photo Electrons, Auger Electrons*

---

[*] corresponding author, eMail: schiwietz(at)helmholtz-berlin.de,
Phone: #49-30-8062-42448 / #49-30--8062-15032

1. Introduction

Electron spectroscopy provides many tools for the investigation of atoms, molecules, clusters and solids. Excitation by electrons, ions or photons enables gaining not only structural information[1], but also detailed insights into electron dynamics, especially if time-resolved measurements are being used. The coupling time of the electronic degrees of freedom with the atomic motion (e.g., lattice vibrations) ranges from 50 femtoseconds (the so-called cold melting[2]) to hundreds of picoseconds via electron-phonon or electron-ion interactions[3]. The electronic motion itself, as e.g. connected to electron diffusion in coordinate space and thermalization of the energy distribution, occurs on a femtosecond time-scale.

Using free-electron-lasers (FEL), x-ray pulses with a width of only a few fs may be used to determine the lattice structure[4, 5] or to investigate short-time dynamics using pump-probe technics[6, 7]. The alternative excitation by primary swift heavy ions is even as fast as 10^{-17} s. Snapshots of the corresponding electronic time-evolution in the range of 1 to 10 femtoseconds may be extracted from the observation of different ion-induced x-ray- or Auger-decay peak-structures.[8] Using pump-probe techniques with FEL radiation or decay-time techniques with fast heavy ions provides high count rates, but it is nearly impossible to avoid high degrees of electronic excitation and the corresponding very high electron temperatures. The perturbative regime at low electron temperatures may be accessed using the so-called femtoslicing techniques, where a small slice of an electron bunch in a synchrotron ring provides x-rays for time-resolved techniques. However, even when combined with an x-ray undulator, this method provides only 10^6 to 10^7 photons per second.[9] Considering the transmission and energy window of the beamline-monochromator, as well as the mean free path (MFP) of electron absorption, Auger yield and MFP of Auger-electron emission from the target, in addition to acceptance solid-angle, transmission, energy window, and detector efficiency of a typical electron spectrometer, we come up with a count rate estimate of far below 0.1 Hz (superimposed on a huge signal background). Such low intensities call for improved electron-spectroscopy methods, when Auger- or photoelectrons shall be measured in a laser-pump/x-ray-probe experiment.

Many different types of electron spectrometers do exist and the experimental evolution continues until nowadays. [10, 11] For an efficient application of electron spec-

troscopy in femtosecond laser-pump/x-ray-probe experiments, however, some further improvements are needed. Thus, we have designed an electron spectrometer that

- features cylinder symmetry, up to 100% transmission and a large acceptance solid-angle for high count rates
- features a good intrinsic time resolution, in order to separate individual bunches within the synchrotron time structure and to minimize the influence of stochastic detector-noise signals
- is insensitive to large amounts of low-energy electrons, as produced by strong pump-laser pulses
- is compact, as well as mechanically and electronically robust.

The above requirements have directed our attention to the so-called Bessel-box design principle. The original version of this electrostatic energy filter for charged particles is termed “Bessel Box”, because its internal electrostatic potential and field strengths depend on the modified Bessel functions of order zero and one[12].

This original Bessel-box version is displayed in Fig 1a. It works similar to a so-called einzel lens that focuses charged particles without changing their exit energy. Ring-shaped entrance and exit apertures define the electron trajectories, corresponding to certain fixed ratios between electron energy E_e and analyzer voltage U. A major disadvantage of the original design, however, is the existence of (asymmetric) trajectories that cross the symmetry axis. These trajectories lead to spurious peaks in the energy spectra and need to be removed. An appropriately improved Bessel-box version[13] is displayed in Fig 1b, as this design avoids such spurious trajectories. Today one may find many applications of different Bessel box types in ion sources, ionization vacuum meters, ion detectors and quadrupole mass spectrometers.[14, 15, 16] In this paper, however, we concentrate on the development of a new and significantly improved Bessel box type (the retarding Bessel box **RBB**) as a stand-alone system enabling electron spectroscopy under extreme conditions. These extreme conditions are low primary electron intensities, a strong low-energy electron background by high-power laser excitation and nanosecond intrinsic timing requirements. Fig 1c shows our new design and, in comparison to the original design, the exit plate is modified in two aspects: It contains only a single exit hole instead of a ring aperture and it is connected electrically to the analyzer voltage U. This design does not allow for trajecto-

ries without cylinder symmetry and it includes other advantages, as will be discussed in the subsequent sections.

2. Experimental methods

The retarding Bessel-box RBB system has been tested inside a mobile ultra-high vacuum (UHV) scattering chamber at residual pressures typically far below 10^{-9} mbar during the various experimental runs. Measurements have been performed with incident electrons, using primary electron energies between 500 eV and 5 keV as delivered by the internal electron gun of the scattering chamber. The main experimental runs have been performed with synchrotron radiation at the dipole beamline PM3 and at the undulator beamlines UE112_PGM-1, UE56-2_PGM-2, and UE56-1_PGM of the BESSY II synchrotron in Berlin.

The spectrometer was mounted on an x/y/z-translation stage, located at a detection angle of 90° with respect to the incident x-ray-beam direction and at 135° (backward scattering) with respect to the incident electron-beam direction. For the electron detection, the RBB was first equipped with a simple anode plate that enables DC electron-current measurements. Later on, a μ-sphere plate and finally a chevron-type double channel-plate (resistivity matched detection-grade type, with an aspect ratio of 60:1 by tectra) have been used for single electron counting as well as event-mode data acquisition (saving the measured pulse height as well as the electron time-of-flight).

Very different types of targets (atomically clean graphite and copper as well as a naturally oxidized Al sample) have been used during the test phases of the RBB. The surfaces of the clean sample have been prepared either by cleaving or by sputter erosion with an internal Ar-ion gun and sample annealing using electron-beam heating. A small aperture at the end of the target holder (below the 3 additional sample positions) is used as a metering orifice. An accurate adjustment of the different primary beams at the same point in space with respect to the target center(s) is performed in connection with the target-current measurement and optical fluorescence inspection at the aperture as well at the exit port of the chamber.

3. Trajectory Simulations

Electron-trajectory simulations have been performed using versions 7.0 and 8.1 of the

SIMION[17] program. The final simulations are based on a 2D grid with cylindrical symmetry and a resolution of 0.1 mm per grid point. The definition of the simulated electrostatic boundary conditions is adjusted to measured distances and size of all electrodes and apertures of our test device. Because charged-particle trajectories depend only on the ratio of kinetic energy and electrode voltage (independent of particle mass), we have performed all simulation with electrons at or around an energy of 1 keV. The central entrance blocker has a diameter of 6 mm in all simulations, corresponding to an angular cone of ±6° or less. This carbon-coated blocker does not only stop electrons from directly hitting the detector, it also absorbs scattered x-ray and laser photons, allowing for pump/probe experiments at high laser power.

The exit aperture of the RBB has also a diameter of 6 mm. Most simulations were performed for a multi-channelplate (**MCP**) behind the exit aperture. The MCP–front voltage V_d is typically +100 V and the MCP–backside voltage is about +2000 V. Note that the calculated electron trajectories are slightly influenced by the value of the MCP–front voltage V_d. An influence of the MCP–backside voltage, however, was not observed.

Fig. 2 displays a 3D presentation of the negative electrostatic potential (potential electron energy) as function of the position inside the RBB. The bundle of red curves shows trajectories of electrons at E_e=1000 eV for an inner spectrometer voltage of V_i =-937 V. The yellow time markers in the trajectory bundle indicate consecutive time-periods of 1 ns. All trajectories start with different polar emission angles θ_e at the same fixed source point on the spectrometer axis. Some of them enter the RBB through the electron-optical entrance aperture ring behind the front inlet (for the suppression of stray electrons). This determines the electron-acceptance angle of the spectrometer. These electrons are decelerated and slightly steered away from the spectrometer axis due to the repulsive potential (during climbing up the potential energy hill). The electron slowing-down is also visible as a reduced distance of the time markers. Afterwards, the electrons are steered back to the axis center and compressed in space (focusing property of the RBB). Finally, the trajectories penetrate the exit aperture and are accelerated onto the front side of the MCP detector (V_d=+100 V), where they may lead to countable electron signals.

Fig. 3 displays the same cut through the spectrometer for three different inner spectrometer voltages V_i. For each value of V_i, equipotential-lines are shown for the

same set of potentials and the plotted electron trajectories belong to same total electron energy (E_e=1000 eV) and to the same set of polar emission angles θ_e. The distance between the electron-source point and the electron-optical entrance aperture RBB ring is Δz=28 mm, as in Fig. 2. Fig. 3a displays the case of high repulsive potentials (V_i =-1037 V) and consequently the 1-keV-electrons cannot pass the exit aperture. The trajectories are even bent backwards and do never penetrate far into the interior of the RBB. Fig. 3b shows the same situation (V_i =-937 V) as in Fig.2, with an optimized voltage at the inner electrode and an electron transmission of about 100%. In Fig. 3c, the magnitude of V_i is so low (-837 V) that the electrons are not completely bent back to the spectrometer axis. None of the electrons do pass the exit aperture and thus, the transmission of the spectrometer is 0 for this case.

Fig. 4 displays the predicted electron yield (for Δz=28 mm, as in Fig. 2) as function of the inner Bessel-box voltage V_i, the so-called spectrometer function. SIMION simulations have been performed for a single fixed source point of 1-keV-electrons (E_i = 1000 eV) and for equidistant mesh points of polar emission angles θ_e. The effective detection solid-angle $\Delta\Omega^{eff}$ is evaluated numerically from the simulated electron trajectories according to

$$\Delta\Omega^{eff} = 2\,\pi\,\sum_i \Delta\,\theta_{e,i}\,\sin\theta_{e,i}\,,$$

where each detector hit with index i is weighted with the corresponding sine of the polar angle $\theta_{e,i}$ and with the fixed polar mesh-point difference $\Delta\theta_{e,i} = 0.01°$. The effective solid-angle $\Delta\Omega^{eff}$ as defined above is simply the product of the constant entrance solid-angle $\Delta\Omega^0$ and the spectrometer-transmission function $T(V_i, E_e)$. The parameter $\Delta\Omega^0$ is the solid angle given by the pure geometrical entrance opening of the spectrometer relative to the source point. The transmission function $T(V_i, E_e)$ is the ratio of electrons behind the exit aperture to the ones that enter the spectrometer field and accounts for the electrostatic interaction between the inner electrode of the RBB and the electrons. Experimentally, one has also to consider the energy-dependent detection efficiency ε (using the equation $\Delta\Omega^{eff} = \Delta\Omega^0 T(V_i, E_e)\epsilon(E_e)$) that is influenced by the choice of the electron-detector system. For the results in Fig. 4, however, we use $\varepsilon = 1$.

As is visible from Fig. 4, the spectrometer function is asymmetric. The mean value of the distribution is $\langle V_i \rangle \approx 943.4\,V$ and the peak maximum of the spectrometer function is found at $V_i^{max} = 936.8\,V$. At this peak maximum nearly all trajectories

that enter the spectrometer through the entrance opening do also pass the exit aperture, corresponding to a transmission of 99.2%. The absolute value of $\Delta\Omega^{eff}$ is 0.106 sr for this case, which means that about 1.7% of all electrons emitted into the hemisphere (limited by a cone of ±12.1°) are analyzed inside the RBB. It is emphasized that even very large electron analyzers in their most recent development stages do just reach the 10% level[10], when considering the reduced transmission through grids as well. The relative energy resolution of the RBB is 2.34% FWHM for the above case. This value is surprisingly small for an electrostatic spectrometer with large openings and without an extra deceleration stage. Focusing and deceleration in front of the exit aperture of this retarding Bessel-box (RBB), however, lead to a high transmission and an increase the energy dispersion, in order to ensure a reasonable energy resolution. Note that the shape of the spectrometer function and the quantitative results derived therefrom do also depend on the distance Δz between RBB and the electron source-point, a parameter that will be varied in the subsequent sections.

4. Results and Discussion

In the following subsections, we present first experimental electron spectra taken with the RBB and evaluated quantitative parameters of the detection system in comparison to values extracted from SIMION electron-trajectory simulations (see section 3). Results for aluminum oxide and for highly oriented pyrolytic graphite (HOPG) will be shown and spectra have been taken with different types of electron detectors: a simple anode plate, a μ-sphere detector and finally with a chevron-type double channel-plate detector. Finally, the spectrometer timing and its ability to cope with pump-laser radiation as well as with the low x-ray flux from a femto-slicing source will be discussed.

4.1. Electron Spectra

Fig. 5 displays an electron spectrum induced by the interaction of primary electrons at a kinetic energy of 800 eV with a cleaved HOPG sample. The x-, y- and z-settings of the RBB had been optimized, prior to the measurement of this spectrum. The distance between target center and RBB entrance-aperture ring was Δz=40 mm, limited by the position of the primary electron beam. The spectral intensity (not corrected for the energy dispersion) was obtained from the electrical current measured at an anode-plate at ground potential (no detector-bias voltage), used instead of an amplifying

detector behind the exit aperture. The low anode-plate current in the fA to pA range set the requirement for a low-pass filter and averaging over at least 1 second, in order to reduce the influence of internal and external electrical noise. Furthermore, it was necessary to delay the current measurement for some seconds after switching to a new Bessel-box voltage, for damping the influence of capacitive cross talk (between inner electrode and anode plate) inside the RBB. This measurement-mode (current integration with an anode plate) does not yield any information on the electron time-of-flight, but it can be used for absolute calibration purposes or for the investigation of extremely high electrons intensities.

The spectrum in Fig. 5 contains different features that are very typical for electron-induced spectra. At the highest Bessel-box voltage, corresponding to the electron energy of 800 eV, the backscattering peak is visible, where the incoming electrons are deflected by the screened target nuclei without any inelastic energy losses. This restricts the penetration depth to about 0.8 nm (between 1 and 2 layers of graphite), 41% of the so-called mean free path (IMFP)[18] for the large backscattering angle of ϕ=135°. Slightly below 800 eV there is a shoulder in the spectrum due to backscattering involving inelastic energy losses, related to excitation of bulk plasmons. At the energy of about 270 eV, there is the carbon KVV Auger-peak structure, where an inner-shell vacancy (K) decays due to the residual interaction of two valence-band electrons (VV). Because the IMFP at 270 eV is only 0.8±0.2 nm[18], the Auger-electron emission tests the same depth as the elastic backscattering. One may use this line structure, e.g., to derive information about the degree of multiple ionization, electronic screening and local electron temperature after ion excitation.[19] The continuous electron intensity below the backscattering and Auger peaks is due to electrons that have suffered many inelastic energy losses related to various processes, e.g., surface- and bulk-plasmon- as well as intra- and inter-band excitations. The energy loss of a fast electron is most likely related to the creation of a slow electron and such cascade electrons pile up in the low energy maximum visible at about 10 eV in Fig. 5.

Fig. 6 displays an electron spectrum induced by the interaction of monochromatic x-rays at a kinetic energy of 360 eV with a native (oxidized) Al sample. The spectrometer is placed at an angle of 90° with respect to the linearly polarized photon beam. The target normal is at an angle of 45° with respect to incident and emission angle, all in the same scattering plane. As in Fig. 5, also this spectrum has been meas-

ured in the current-integration mode without any detector bias. The distance between target center and RBB entrance-aperture ring was Δz=34.5 mm, the shortest possible distance for an x-ray generated spectrum with our RBB test-version. As this is a native Al sample, it contains not only Al, but also O and C. Thus, there are different types of photo-electron peaks (marked XPS) and a carbon KVV Auger peak, as in Fig. 5. The clear separation of the different peaks shows that a stoichiometry analysis is possible with the RBB in combination with a corresponding software package[1]. The anode peak-current of the Al-L_{23} peak is slightly below 2 pA, corresponding to 10^7 electrons/second. The current fluctuation is about 1% of the mean current at Bessel-box voltages between 100 and 200 V. These fluctuations are due to electronic amplification and due to external noise signals. In a pulse-counting mode this would correspond to a statistical noise of only 10^4 electron counts in the Al-L XPS peak.

4.2. RBB Parameters

Fig. 7 displays two energy-calibration curves of the RBB. The distance between target center and entrance aperture RBB ring was Δz=30.5 mm in this case. Several photo-electron spectra have been taken for native Al and Si samples, similar as in Fig. 6. The open blue diamond symbols on the upper calibration curve are derived from the relative Bessel-box voltages corresponding to the Al-L_{23} photo-ionization peak maximum vs. the primary photon energy in the current-integration mode. The red circles have been obtained for the same oxidized Al sample, but using pulse-counting with electron-cascade amplification by a μ-sphere-plate (MSP) detector. In both cases, the photon energy of 200 eV was taken as reference energy. The olive solid circles are taken for a Si target and rely also on pulse-counting with the MSP detector. It is seen that the slope of the calibration relation, V_i vs. E_{photon}, does neither depend on the target nor on the detection method. A spectrometer constant C_{RBB}, with

$$C_{RBB}(\Delta z = 30.5\ \text{mm}) = \frac{V_i}{E_{electron}} = \frac{\Delta V_i}{\Delta E_{photon}} = 0.9426 \pm 0.0007$$

may be extracted from these data points.

Fig. 8 displays important characteristic values of the Bessel-box spectrometer. Three measured and simulated dependencies are plotted as function of the z-distance Δz_{RBB} between the source point and the electron-optical entrance-aperture. The effective detection solid-angle $\Delta\Omega^{eff}$ is shown in Fig. 8a). The solid green diamonds (con-

nected by a spline curve) have been computed with SIMION, as explained for Fig. 4. In Fig. 8a), however, we present only the solid angle for the maximum electron yield, after optimization of the Bessel-box voltage V_i. It is seen that a maximum detection solid angle of about 0.1 sr may be reached at z-distances below 30 mm. Compared to the value of 2π for the hemisphere, this means that nearly 2% of all electrons ejected from a surface are analyzed in the RBB. The dashed green curve shows the typical relative Δz_{RBB}^{-2} dependence of $\Delta\Omega^{eff}$. Deviations from the Δz_{RBB}^{-2} dependence are found at small ($\Delta z_{RBB} < 29\,mm$) as well as at large distances ($\Delta z_{RBB} > 55\,mm$). At large distances, the circular background-suppression aperture in the entrance nose (close to the source point, on the right-hand-side in Figs. 2 and 3) blocks the trajectories for large polar angles. This results in a reduced solid angle for the electron-optical entrance into the spectrometer. At small distances, there exists no such external trajectory-blocking, but at $\Delta z_{RBB} < 29\,mm$, the electron transmission is less than 100% inside the spectrometer. This reduced transmission is related to incomplete focusing of trajectories through the exit aperture in the exit plate.

Experimental data are obtained only for the intermediate range of Δz_{RBB} positions. The results are shown as solid pink stars and they have been determined from the maximum measured relative photo-electron peak intensity (see Fig. 6) by varying Δz_{RBB} and keeping all other experimental parameters fixed. These intensity values are adjusted to the theoretical results in Fig. 8a). Comparison of RBB measurements using anode-plate electron-detection with the total target-emission current shows that the experimental detection solid-angle $\Delta\Omega^{eff}$ is consistent with the SIMION results in Fig. 8a).

Fig. 8b) displays the relative electron-energy resolution $\Delta E/E$ of the RBB, where E is the measured kinetic energy of a sharp peak and ΔE is the corresponding FWHM energy width. The solid pink stars are experimental data derived from Al-L_{23} photo-electron peak-shapes, as in Fig. 6. The solid blue hexagons are experimental data points derived from the high-energy slope of electron backscattering at 1000 and 800 eV, as in Fig. 5. The small solid olive squares connected by a curve have been estimated from SIMION calculations using simplified assumptions on the simulated peak shapes. The two larger solid olive diamonds show accurate SIMION results obtained from full peak-shape analyses for two z-positions (Δz = 28 mm as in Fig. 4 and 46 mm). Comparison shows that the measured energy resolution seems to be slightly

better than the one obtained from the trajectory simulations. A misalignment of the absolute target-spot position, and hence an error in Δz, might be an explanation, although our estimated Δz-uncertainty of ±1 mm is somewhat too low to explain the deviations in Fig. 8b).

Fig. 8c) displays the spectrometer constant (or spectrometer factor) C_{RBB} as function of the spectrometer-target distance Δz_{RBB}. The spectrometer factor describes the relation between measured kinetic electron-energy $E_{electron}$ and the inner Bessel-box voltage V_i, as discussed for Fig. 7 ($C_{RBB} = V_i/E_{electron}$ [V/eV]). The experimental photo-electron results are shown as solid pink stars, as in Fig. 6. The precise data point at Δz=30.5 mm is extracted from the energy-calibration curves in Fig. 7. Other data points involve only two or three measurements at different x-ray energies. The dashed pink curve was obtained from experiments at just one photon energy as function of the distance Δz_{RBB}, and thus, this curve is scaled to the other (absolute) experimental data. The solid blue hexagons are experimental data points derived directly from electron backscattering, as in Fig. 5 (by assuming a good absolute accuracy of the electron gun in use). As in Fig. 8b), the small solid olive squares plus curve show simplified estimates of the spectrometer factor for a reduced set of SIMION calculations and the two larger solid olive diamonds show accurate SIMION results obtained from full peak-shape analyses for the mean inner Bessel-box voltage $< V_i >$ for two z-positions (Δz = 28 mm as in Fig. 4 and Δz = 46 mm). All spectrometer factors are slightly below 1, which means that the inner Bessel-box voltage (in Volts) is only slightly lower than the kinetic electron energy (given in eV). The absolute experimental and theoretical spectrometer factors agree well with each other. Time-dependent RBB properties are discussed in the section below.

4.3. Time-of-Flight Distributions and Short-Time Test

Fig. 9 displays three simulated electron time-of-flight spectra for the RBB as function of the absolute flight time of 1-keV electrons. Each distribution $d^2N/d\Omega dt$ was determined from a sampling (weighted with $\sin\theta_{e,i}$) of the absolute flight times calculated with SIMION (time bins are 0.02 ns wide) for trajectories that reach the front surface of the detector. Going beyond the single-source-point approximation, we have performed these simulations for a set of 9 different source points representing a source diameter of about 90 μm. In each case, the original data are plotted as symbols and a

fit curve with equal color is added to guide the eye.

The solid pink circles have been obtained for a distance of Δz = 46 mm and for an optimized Bessel-box voltage of -922.0 V. The other two data set have been calculated for Δz = 28 mm (as in Fig. 4). Although the mean time-of-flight varies only by 0.8 ns out of about 18.5 ns (4% variation) for the two distances, the width does strongly depend on the distance (FWHM of 0.61 ns and 1.11 ns for the two cases). The pink symbols (Δz = 46 mm, V_i=-922.0 V) correspond to a transmission of 100%. This is not the case for the other two curves. The solid blue squares (Δz = 28 mm, V_i=-937.2 V) correspond to a transmission of 98.2%.

This distribution has an asymmetric shape with a sharply rising onset and a continuously decaying behavior at larger times, similar to the pink curve. The blue curve, however, is influenced by 1.8% of the particles that are blocked by the exit plate, close to the aperture. These trajectories correspond to long flight-times and large initial polar angles. The olive curve (solid green diamonds for Δz = 28 mm, V_i=-936.8 V), however, looks different although the inner voltage differs by only 0.4 V from the blue curve. This olive curve corresponds to a reduced transmission of 95.6% and the missing trajectories are found at intermediate flight times, producing a dip in the time spectrum. These intermediate flight times are related to intermediate initial polar angles and the focusing properties of the RBB are causing other trajectories to penetrate the exit aperture. Hence, small variations of the inner voltage may have a significant effect on the shape of the time-of-flight spectrum for a mono-energetic line.

Fig. 10 displays measured time-of-flight distributions dN/dt as function of a channel number (in arbitrary units) for a distance of Δz = 30.5 mm. The Al-$L_{2,3}$ photo-ionization peak has been selected by the choice of two primary photon energies ($E\gamma$= 200 eV and 670 eV) and the corresponding Bessel-box voltages (-175 V and -554 V). The time difference between an electron-signal processed by a constant-fraction discriminator and the BESSY-II synchrotron-bunch-marker provides the (relative) time-of-flight value. Electronically, this time difference is converted into a pulse height with a time-to-amplitude converter (TAC) and this analogue signal is digitized by an analog-to-digital converter (ADC) within our setup.

Measurements have been performed with different time ranges Δt-TAC. At Δt-TAC = 2 μs in the lower part of figure, the periodic time structure of the synchrotron

(repetition frequency of 1.25 MHz corresponding to an 800-ns period) is clearly visibly. It is related to the so-called multi-bunch-(3+1)-hybrid-mode, the standard operation mode for femtosecond slicing operation at BESSY II. This mode includes a multi-bunch train with many small electron bunches being 2 ns apart and carrying 280 mA of electron-beam current altogether. This multi-bunch train corresponds to the flat parts of the time distribution at channel numbers below 166 and above 286. The multi-bunch train is interrupted by a gap of about 225 ns, containing only four larger pulses. These so-called single bunches carry a maximum electron current of 5 mA each and are separated by 36 ns from each other.

The upper two plots in Fig. 10 show the same synchrotron-time structure as below, but at a higher Bessel-box voltage and with reduced TAC ranges (Δt-TAC = 200ns and 50 ns) in order to expand the time scale and to improve the time resolution of the RBB as well as of the electronics. In the central plot, one may clearly observe the 36 ns distance between the large single bunches and in the upper plot it is even possible to observe the 2-ns pulse separation in the multi-bunch train. An experimental time resolution of $\Delta t=1.9\pm0.2$ ns may be extracted from this plot. At the RBB electron energy of about 590 eV, we expect the time-of-flight value and peak width to be increased by a factor 1.30 (proportional to $E^{-0.5}$) in comparison to the SIMION simulations in Fig. 9. Using a geometrical interpolation of the Δz values, the electronic time resolution and the known energy scaling we estimate a FWHM value of $\Delta t=1.6$ ns. Taking into account that the SIMION results in Fig. 9 have been obtained for mono-energetic electrons, this estimated time resolution is in good agreement with our experimental value. Even the asymmetry of the simulated peak structure seems to be reflected in the measured time spectra. Furthermore, the Δt values are roughly doubled, when a flat continuous electron distribution (no sharp energy peak) is selected with the RBB. This statement holds true for the experimental data (not shown in Fig. 10) as well as for the SIMION analysis of such a case.

In the last part of this section, we will show that the electron count-rates are high enough and detector background is low enough to perform even slicing experiments with this setup. In principle, our data-acquisition system is able to produce event mode data, where the electron energy, the detector pulse-height as well as the time-of-flight value are stored together for each detected electron, enabling accurate post-beam-time evaluation. In the following, however, we have simply used pulse-

height discrimination of the TAC pulse to define an electron acceptance-time-window of a roughly 10 ns width. Thus, we are counting those electrons that reach the detector within a pre-defined time-window related to the range of electron energies to be measured in a spectrum. A time-window being too small would suppress true electrons counts, but the larger the time window is, the more electron-signals from neighboring synchrotron bunches as well as statistical detector-noise signals would lead to an unwanted background count rate.

Fig. 11 displays two electron spectra taken under extreme experimental conditions. Photons of an energy of 940 eV have been directed onto an atomically clean Cu (110) target under grazing incident angles. The emission angle in this case is close to the surface normal. Thus, we have optimized the excitation conditions (grazing Cu-L_3 ionization slightly above the edge) and the emission condition for a maximum count rate. The electron energy range corresponds to the Cu-LMM structure that is superimposed on the weaker photo ionization peaks from valence band and M shells. X-ray excitation of Cu and Cu-LMM Auger-electron emission is well investigated[20], specifically for excitation close to the L_3 resonance[21].

The symbols represent uncorrected experimental data taken during a pulse-sampling time of 150 s for each data point. The underlying curves are fits to guide the eye. The upper curve is actually very similar to spectra taken with a large fraction of the synchrotron beam at electron count rates of nearly 1 MHz. The detected count rate in Fig. 11, however, was only 0.7 Hz or less. In order to extract short x-ray pulses of a width of only 100 fs, the BESSY femto-slicing facility was used for the upper spectrum. These femto-slicing x-ray pulses are produced with a frequency of only 6 kHz, compared to 500 MHz within the BESSY multi-bunch train. Using laser-induced modification of a synchrotron bunch inside an undulator, a 100-fs slice is cut out of a 100-ps bunch. Considering all such loss effects, femto-slicing x-ray-pulses are reduced by roughly a factor of $4 \cdot 10^{-8}$ compared to the full beam (at low time resolution). At such a low x-ray flux, statistical noise in the detector or an x-ray background of slow pulses due to insufficient filtering in the beamline may become important. Both background sources, however, can be excluded based on the low counting rate in the lower spectrum of Fig. 11. This spectrum is taken under identical conditions as the upper spectrum, but with the femto-slicing pulse extraction being switched off. Thus, the RBB is able to operate nearly background-free under femto-slicing conditions at the BESSY-II synchrotron.

5. Conclusions and Outlook

We have developed a new and compact type of electron spectrometer, optimized for special tasks in surface science. With its small length of about 15 cm, it may be even mounted inside a scattering chamber. Our actual version of the RBB features a large detection solid angle (nearly 2% of the hemisphere for ejection from solid surfaces), a total time resolution of about 2 ns, and a relative energy resolution of about 3%. For all important RBB spectrometer parameters, experiments and SIMION simulations have been performed and good agreement has been found. This indicates a good understanding of the operation principle of the RBB system. The robust design of the RBB enables the measurement of kinetic electron energies up to about 5 keV.

The large solid angle yields extremely high electron intensities and enables to operate the RBB even in a *current-measurement-mode*, using an anode plate without amplifying detector. A small positive bias voltage at the anode plate should allow for direct absolute intensity calibration of the whole system as the electron-detection efficiency should be close to 100%. The current-measurement-mode enables also a system operation at mbar pressures, as the limiting factor will be electron scattering at residual gas atoms inside the spectrometer and a resulting loss of the electron-energy resolution (this mode has not been tested). Contrary, an open electron detector with cascade amplification, such as electron multiplier, channeltron, microsphere-plate or microchannel-plates, requires a pressure typically below 10^{-5} mbar and thus, is the main limitation regarding residual-gas pressure.

We have tested the RBB also in a *pulse-counting-mode* with a microsphere-plate (el-mul type 025D) and finally with microchannel-plates (tectra MCP25-60 type). This last mode of operation allows electron detection at 0.7 MHz without significant saturation effects. This high count rate enables rapid energy scans as well as NEXAFS scans in a partial-yield mode. The main goal, however, was the development of a spectrometer optimized for laser-pump/x-ray-probe experiments with good time resolution. We have tested the RBB successfully in such measurements with ps time resolution[22]. The spectra of Auger and photo-ionization peaks were not disturbed by Laser induced electrons that pile up at lower energies. Furthermore, we have shown that the spectrometer works well with the low x-ray intensities delivered by the BESSY-II femto-slicing facility, involving short x-ray pulses of only 100 fs width. A

good time resolution of the RBB itself is very important to achieve a low signal background.

Note that the electronic noise of the system has been reduced significantly after finishing the experiment series described here. In addition, *event-mode data acquisition* has later-on been tested as well and thus, the detection time window may now be adjusted to the detected electron energy. Both developments allow for virtually background-free measurements at electron detection rates far below 1Hz. Additional SIMION studies indicate that it is also possible to increase the effective detection solid-angle, and thus the all-over count rate, without a significant loss in time- or energy resolution of the RBB.

In summary, we have developed a new type of electrostatic electron spectrometer, the retarding Bessel box. It is robust and small, involves a large detection solid-angle and the important electron-optical parameters are well understood. We have also shown that the RBB is insensitive to the large number of low-energy electrons and photons produced during laser-pump/x-ray-probe measurements. Finally, this RBB has also passed the test with particularly short and therefore relatively weak x-ray pulses at the femto-slicing facility. Thus, the RBB opens some new tracks for electron-spectroscopy applications.

Acknowledgements

We are indebted to the BESSY-II-synchrotron crew and to N.Pontius, T.Kachel, K.Holldack, and W.Mahler for providing excellent x-ray operating conditions at the different beamlines (UE112_pgm-1, UE56/1_pgm, PM3, UE56/2_pgm-2). One of us (G.S.) acknowledges helpful discussions with and comments by P.L.Grande as well as the motivation by A.Föhlisch for writing up this paper. Last but not least, we should mention the help of two HZB mechanics workshops and specifically of T.Blume and U.Stettner regarding the mechanical design, the fabrication and stepwise optimization of the Bessel-box system.

Figures and Figure Captions

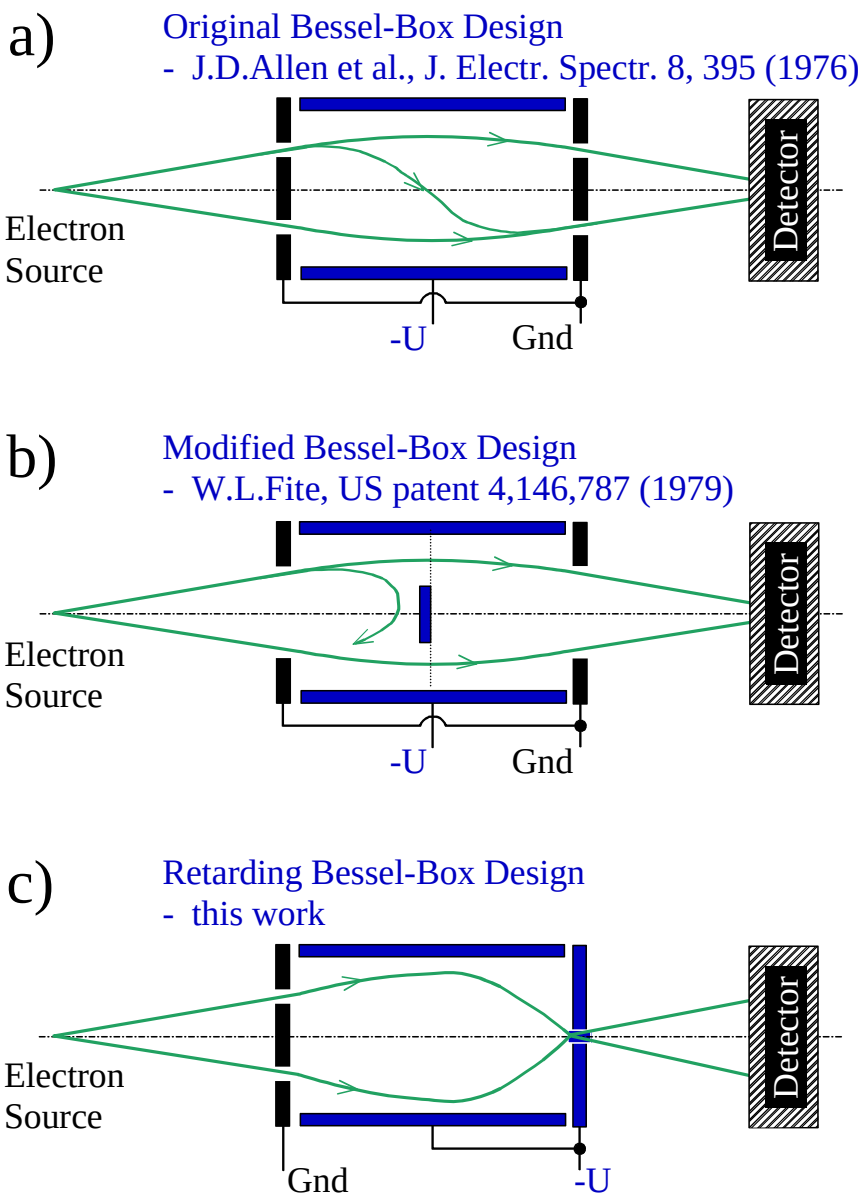

Fig. 1: (colour online) Variations of Bessel-box type energy filters: a) the original and most simple Bessel-box design; b) an improved design with a central electron-stopper plate; c) our improved spectrometer design. The thin (green) curves with arrows show typical electron trajectories corresponding to the specific design.

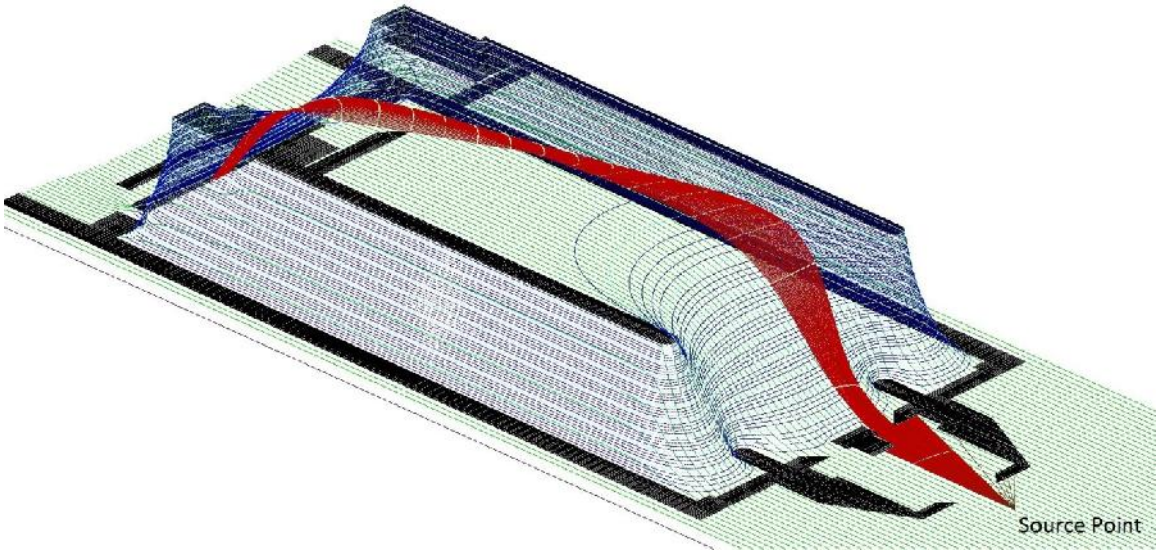

Fig. 2: (colour online) 3D presentation of the electrostatic potential energy *-eV(z,x)* of electrons in the RBB spectrometer. One may see that the outer housing and the front nozzle (near the electron source point) is on ground potential. 1-keV-electron trajectories are plotted as thin red lines, interrupted by (yellow) time markers (see text). After moving through a ring-shaped entrance opening, electrons are decelerated, steered and partly refocused by the repulsive potential (-937 V) on the inner electrode. Finally, after penetrating the exit aperture, electrons are accelerated towards the positively biased detection system (either an anode plate or a pulse-amplification detector).

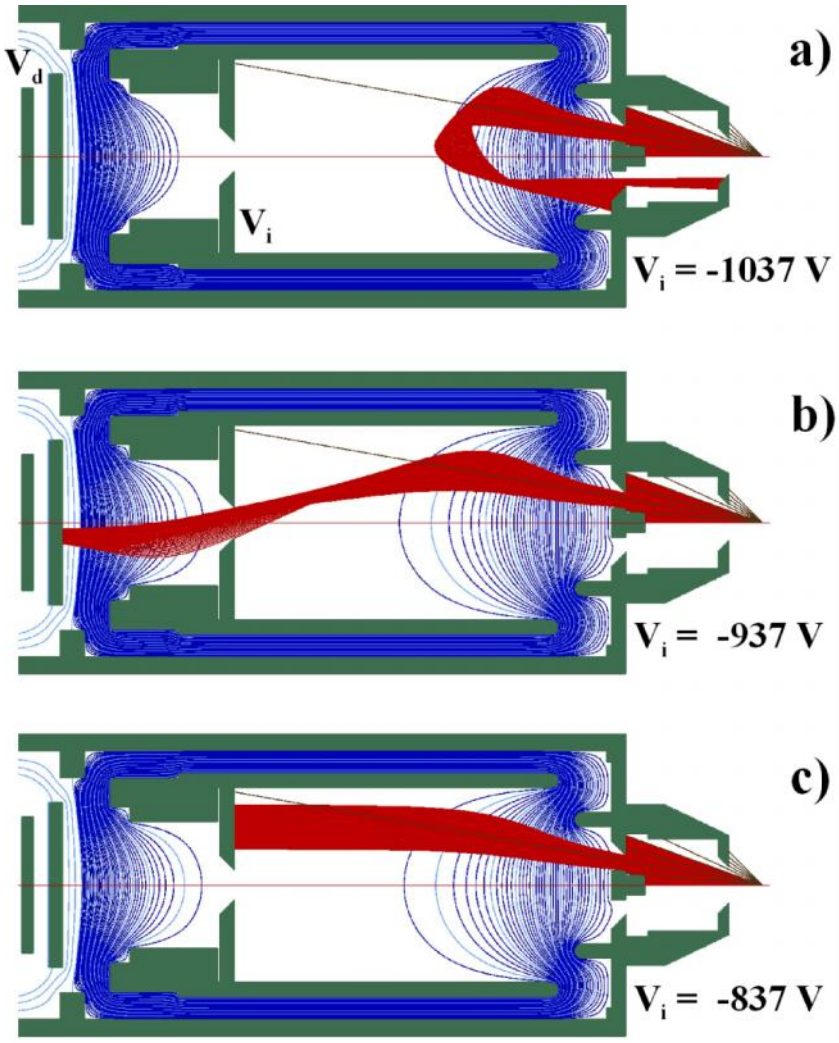

Fig. 3: (colour online) A cut through the RBB spectrometer, showing equipotential lines as thin (blue) curves and a selected group of electron trajectories as a thick (red) bundle for three different retarding voltages V_i at the inner electrode: a) V_i= -1037 V; b) V_i= -937 V; c) V_i= -837 V. All simulated electrons start exactly at the same source point with a kinetic (or total) energy of 1 keV.

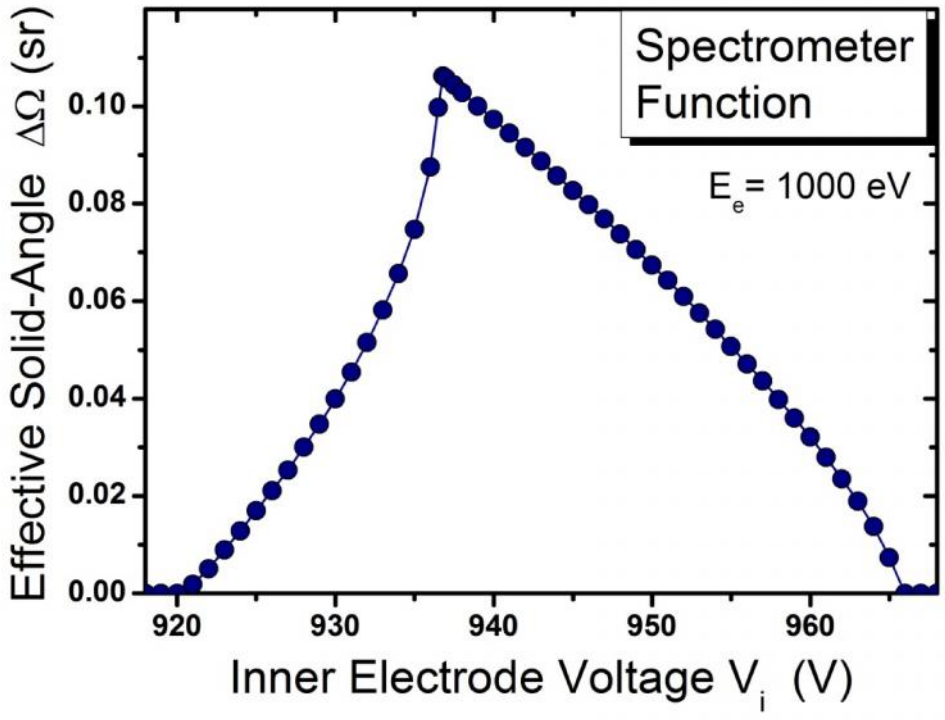

Fig. 4: (colour online) Effective detection solid-angle as function of the Bessel-box voltage, evaluated from detector hits of the simulated electron trajectories (see text).

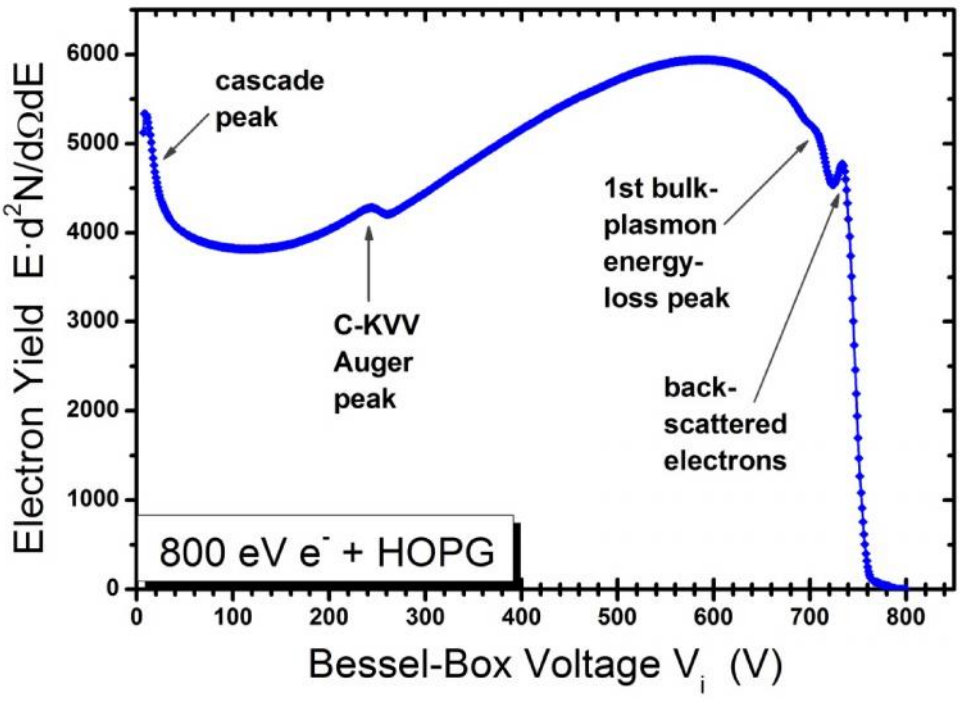

Fig. 5: (colour online) Measured electron-emission spectrum (in arbitrary units) induced by 800-eV primary electrons incident on a cleaved HOPG sample. The backscattering angle is ϕ=135° relative to the incident beam.

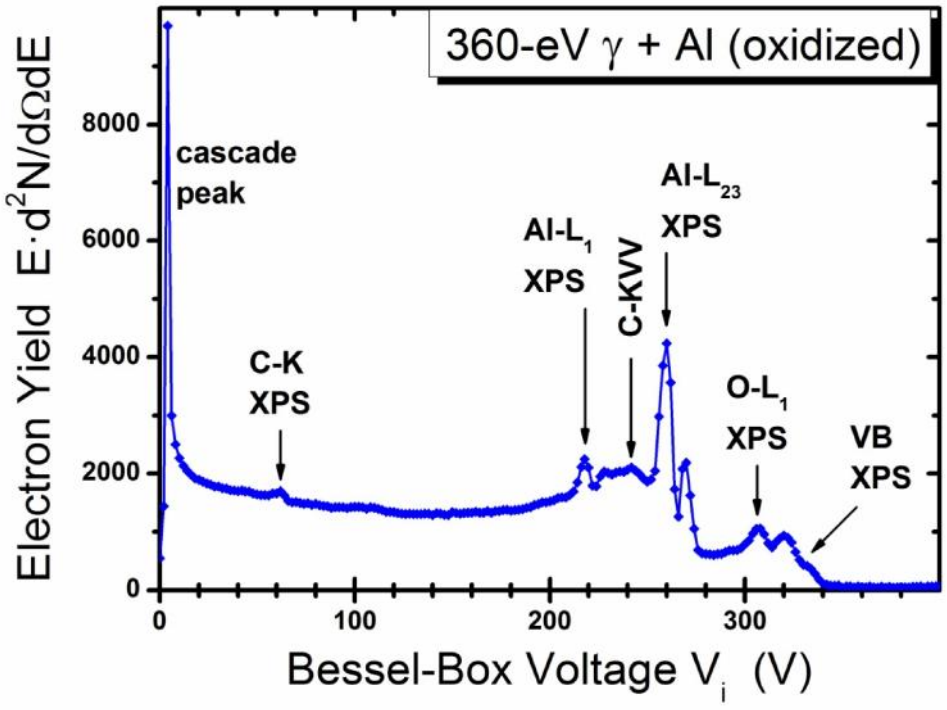

Fig. 6: (colour online) Measured electron-emission spectrum (in arbitrary units) induced by 360-eV primary photons incident on a native oxidized Al sample. The incident and emission angle are 45° in the horizontal scattering plane.

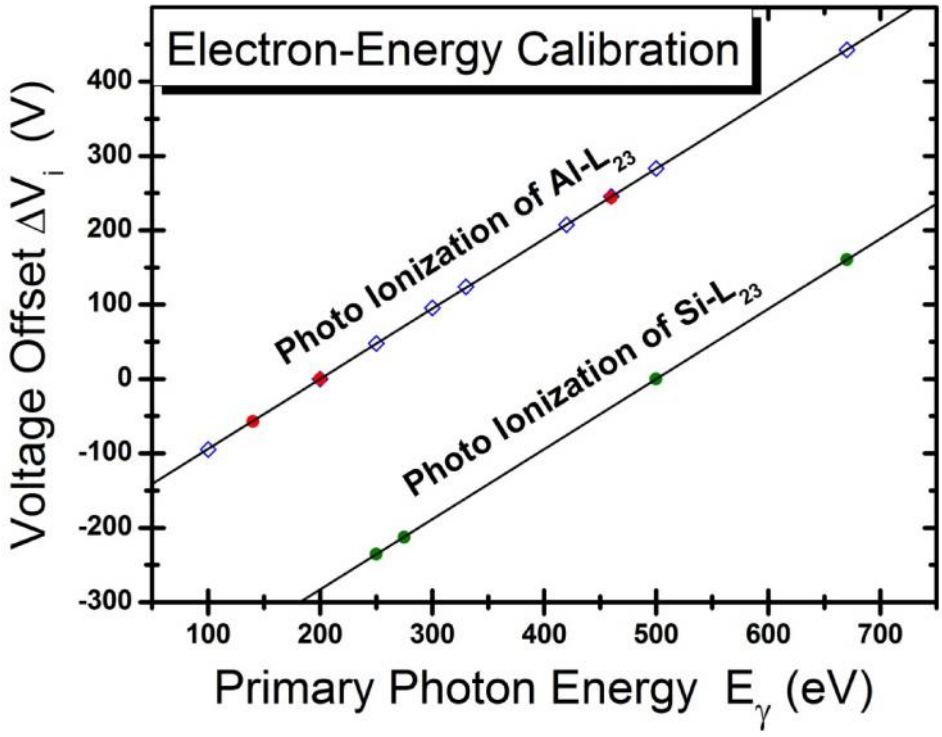

Fig. 7: (colour online) Energy-calibration curve: mean Bessel-box voltage (minus an arbitrarily fixed bias voltage) corresponding to a specific photo-ionization peak maximum vs. primary photon energy (see text).

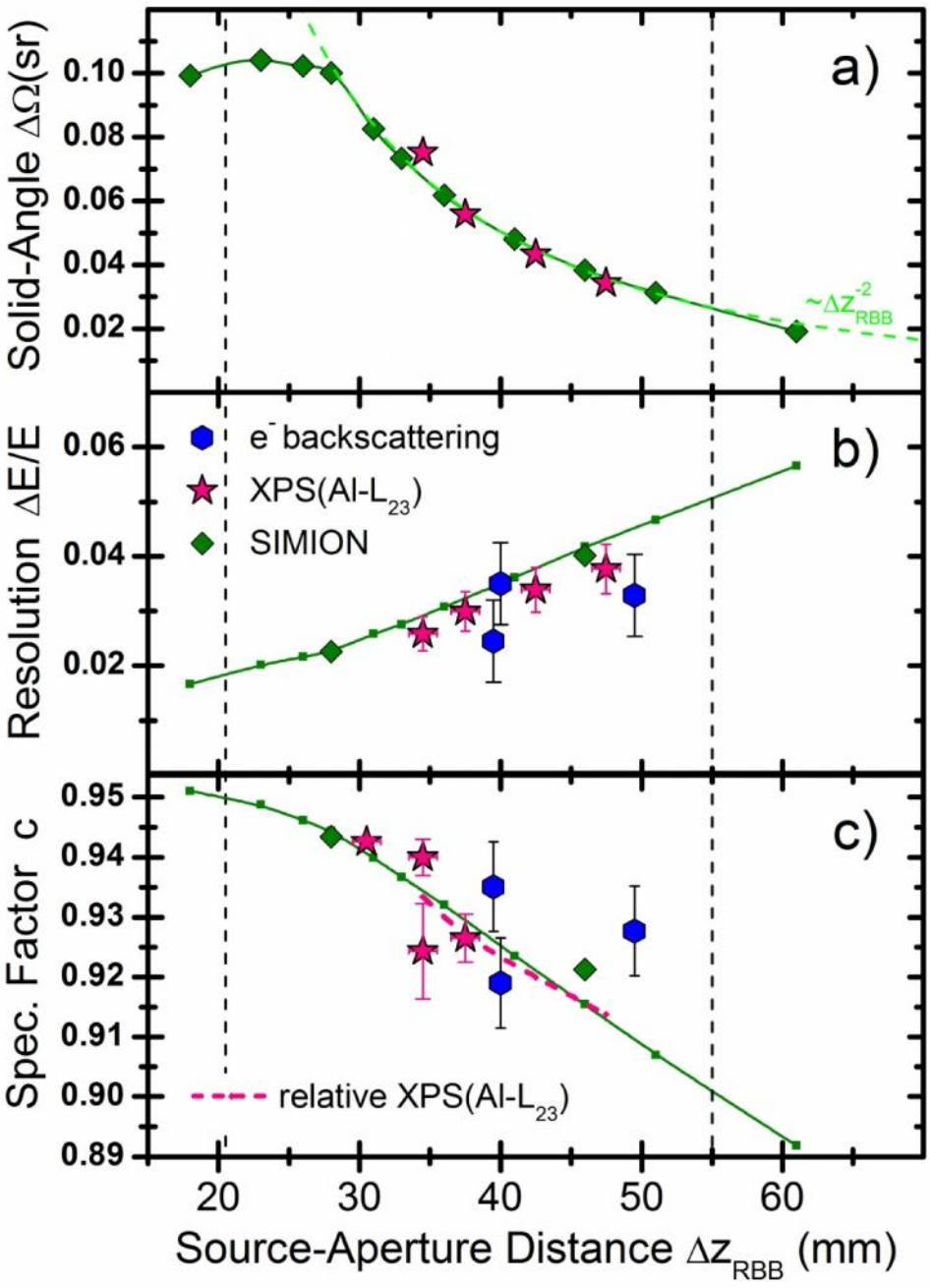

Fig. 8: (colour online) Measured and simulated characteristics of the Bessel-box system for different z-positions of the RBB manipulator. a) Effective detection solid-angle $\Delta\Omega^{eff}$, b) relative electron-energy resolution ΔE/E, and c) spectrometer factor C_{RBB} as function of the spectrometer-target distance Δz (see text). The dashed vertical lines mark the position of the entrance nose (at 20.5 mm) and for those source points (> 55 mm) where large-angle trajectories are blocked by the entrance nose.

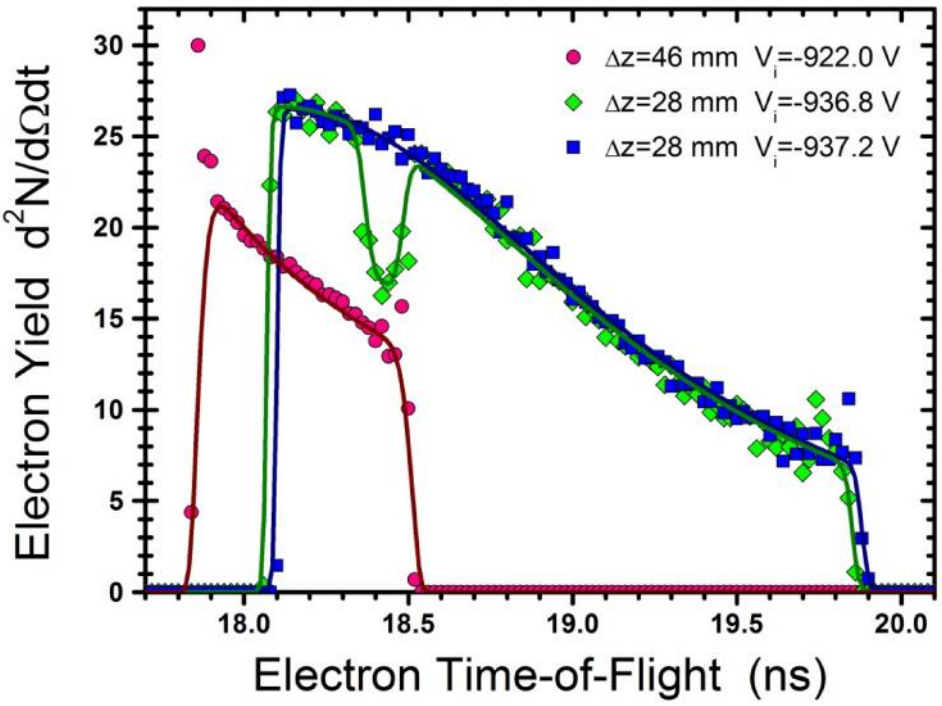

Fig. 9: (colour online) Simulated time-of-flight distribution $d^2N/d\Omega dt$ versus the absolute flight time of 1-keV electrons for a) a Bessel-box voltage of -922.0 V and a z distance of 46 mm (solid red circles), b) a Bessel-box voltage of -936.8 V and a z distance of 28 mm (solid green diamonds), c) a Bessel-box voltage of -937.2 V and a z distance of 28 mm (solid blue squares).

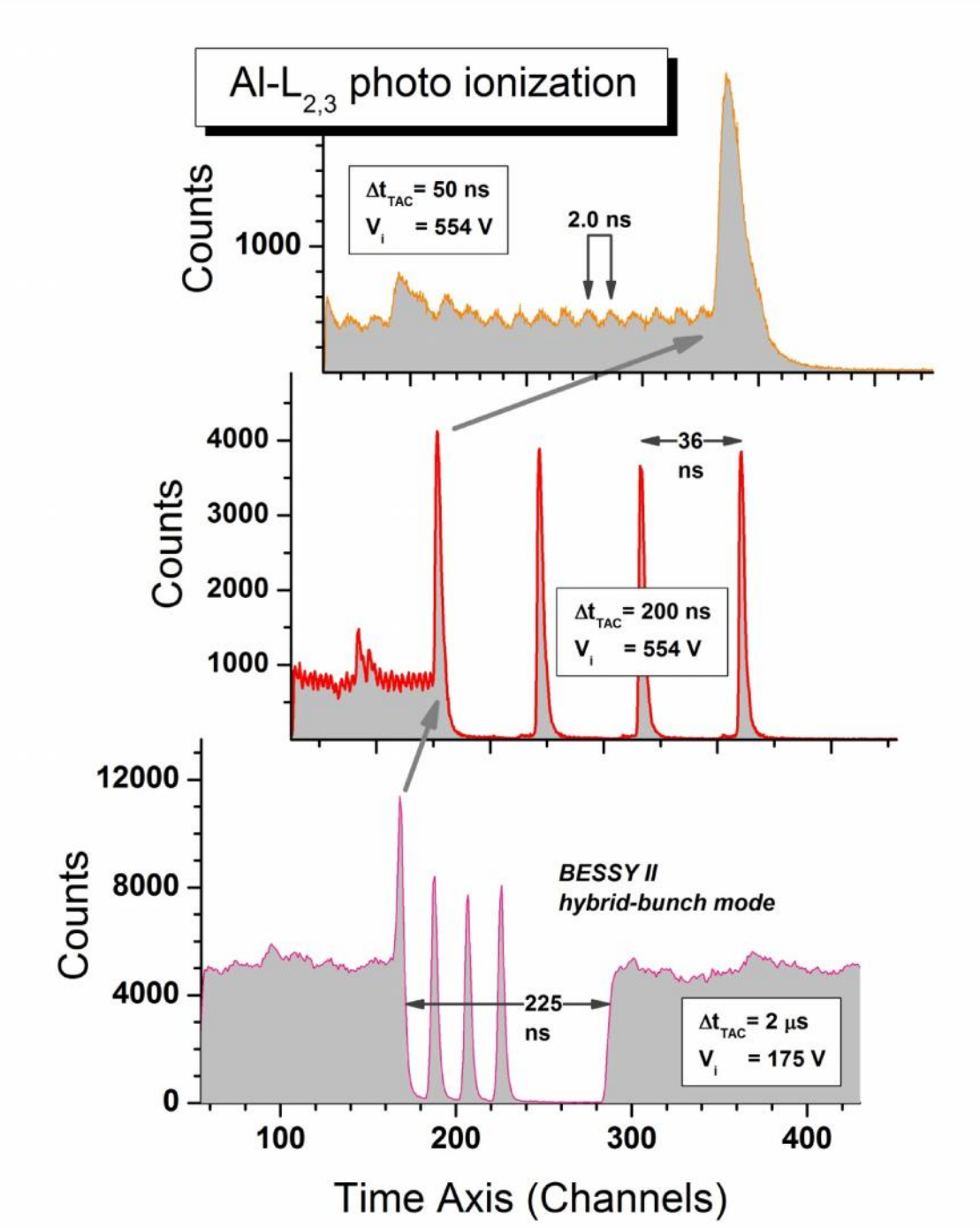

Fig. 10: (colour online) Measured time-of-flight distributions $d^2N/d\Omega dt$ versus channel number for the Al-$L_{2,3}$ photo-ionization peak (at Bessel-box voltages of V_i= -175 V and -554 V) induced by the pulsed x-ray photons delivered by the BESSY II synchrotron. Measurements have also been performed with smaller time ranges (upper two plots) of the time-to-amplitude converter (TAC), in order to improve the electronic time resolution.

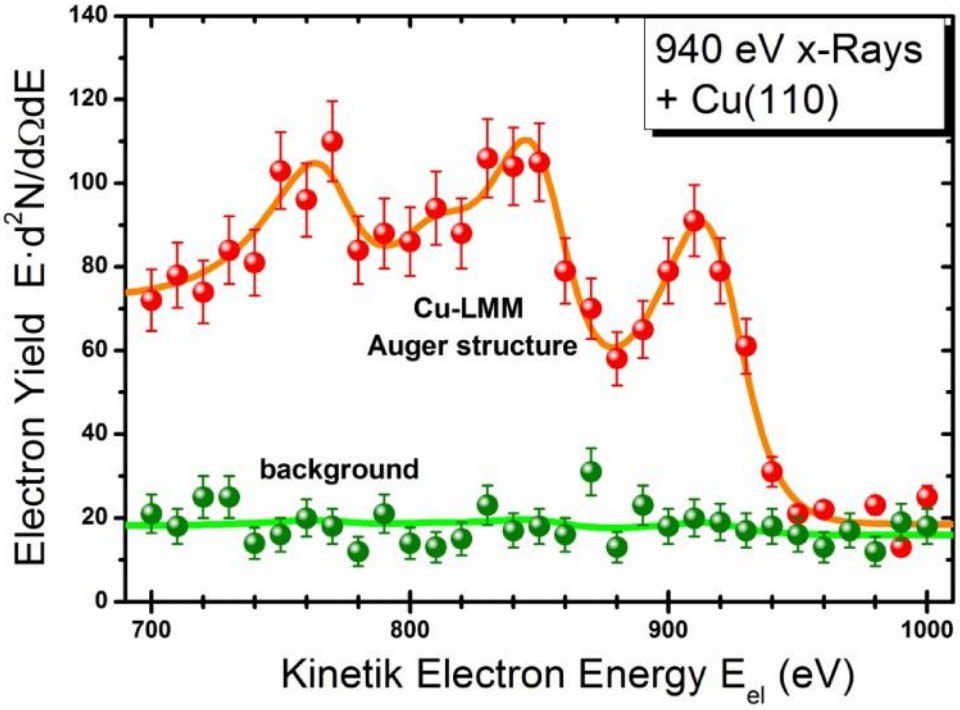

Fig. 11: Measured electron-emission spectrum induced by 940-eV primary photons (slightly above the Cu–L_3 excitation threshold) incident under grazing angles on an atomically clean Cu(110) sample (the emission direction is close to the exit normal exit). The upper spectrum (solid red spheres) is due to the short-time pulses of about 100 fs produced by the BESSY femto-slicing facility. The lower spectrum (solid green spheres) shows the over-all background count-rate, when the laser-controlled femto-slicing x-ray-pulse extraction is switched off. The data acquisition time was 150 s for each energy point in both spectra.

References

[1] NIST Standard Ref. Database **100** for the *Simulation of Electron Spectra for Surface Analysis* (SESSA 1.1); see also W. Smekal, W. S. M. Werner, and C. J. Powell, Surf. Interface Anal. **37**, 1059 (2005).

[2] P. Stampfli, K.H. Bennemann, *"Time dependence of the laser-induced femtosecond lattice instability of Si and GaAs: Role of longitudinal optical distortions"*, Phys. Rev. **B49**, 7299 (1994); P. Stampfli, *"Electronic excitation and structural stability of solids"*, Nucl. Instr. and Meth. **B107**, 138 (1996).

[3] Z.G.Wang, Ch.Dufour, E.Paumier, and M. Toulemonde, *"The S_e sensitivity of metals under swift-heavy-ion irradiation: a transient thermal process"*, J. Phys. Condens. Matter 6 (1994) 6733-6750 and references therein

[4] H.N. Chapman et al., *"Femtosecond diffractive imaging with a soft-X-ray free-electron laser"*, Nature Physics **2** (2006) 839 – 843.

[5] M.E. Couprie, *"New generation of light sources: Present and future"*, Journal of Electron Spectroscopy and Related Phenomena **196** (2014) 3–13

[6] U. Frühling et al., *" Single-shot terahertz-field-driven X-ray streak camera "*, Nature Photonics **3** (2009) 523 – 528.

[7] S. Hellmann, K. Rossnagel, M. Marczynski-Bühlow, and L. Kipp, *"Vacuum space-charge effects in solid-state photoemission"*, Phys. Rev. **B79**, (2009) 035402; S Hellmann, C. Sohrt, M. Beye, T. Rohwer, F. Sorgenfrei, M. Marczynski-Bühlow, M. Kalläne, H. Redlin, F. Hennies, M. Bauer, A. Föhlisch, L. Kipp, W. Wurth and K. Rossnagel, *"Time-resolved x-ray photoelectron spectroscopy at FLASH"*, New Journal of Physics **14** (2012) 013062

[8] G. Schiwietz, M. Roth, K. Czerski, F. Staufenbiel, and P.L. Grande, *"Femtosecond Dynamics: Snapshots of the Early Ion-Track Evolution"*, Nucl. Instr. Meth. **B226** (2004) 683–704; and references therein; G. Schiwietz, K. Czerski, M. Roth, P. L. Grande, V. Koteski, and F. Staufenbiel, *"Evidence for an Ultrafast Breakdown of the BeO Band Structure Due to Swift Argon and Xenon Ions"*, Phys. Rev. Lett. **105** (2010) 187603.

[9] S. Khan, K. Holldack, T. Kachel, R. Mitzner, and T. Quast, *"*Femtosecond Undulator Radiation from Sliced Electron Bunches*"*, Phys. Rev. Lett. **97**, (2006) 074801; K. Holldack, S. Khan, R. Mitzner, and T. Quast, *"Femtosecond terahertz radiation from femtoslicing at BESSY"*, Phys. Rev. Lett. **96**, (2006) 054801.

[10] A.Vollmer, R. Ovsyannikov, M. Gorgoi, S. Krause, M. Oehzelt, A. Lindblad, S. Svensson, P. Karlsson, M. Lundvuist, T. Schmeiler, J. Pflaum, N. Koch, N. Mårtensson, *"Two dimensional band structure mapping of organic single crystals using the new generation electron energy analyzer ARTOF"*, J. Elec. Spectr. Rel. Phenom., **185** (2012) 55-60; R. Ovsyannikov and D. Kühn, private communication (2014); see also the description by VG SCIENTA of the ARTOF-2 electron spectrometer (http://www.vgscienta.com/_resources/File/ARTOF-2%20data%20sheet%20v1.0%20web.pdf).

[11] G. Schiwietz, M. Roth, and F. Staufenbiel, *"Elektrostatischer Energieanalysator für geladene Teilchen, Spektrometer und Monochromator mit einem solchen Analysator"*, German patent 10 2008 058 144 (2011).

[12] J.D. Allen Jr., J.D. Durham, G.K. Schweitzer, W.E. Deeds, *"A new electron spectrometer design: II"*, J. Electron Spectrosc. Relat. Phenom. **8** (1976) 395; J.D. Allen, Jr., J.P. Wolfe and G.K. Schweitzer, A new electron spectrometer design, Int. J. Mass Spectrom. Ion Phys. **8** (1972) 81-83.

[13] W.L. Fite, *"Methods and apparatus for energy analysis and energy filtering of secondary ions and electrons"*, United States Patent 4 146 787 (March 27, 1979).

[14] J.H. Craig Jr. and W. G. Durrer, *"Transmission characteristics of a cylindrical energy analyser"*, Journal of Vacuum Science & Technology **A7** (1989) 3337.

[15] H. Yoshikawa and R. Shimizu, *"A New Bessel-Box Energy Analyzer for Sputtered Neutral Mass Spectrometry"*, Jpn. J. Appl. Phys. **29** (1990) 386-391.

[16] P. Downie, D.J. Reynolds, and I. Powis, Parallel, *"Multichannel energy and angle resolving electrostatic electron analyzer"*, Review of Scientific Instruments **66**, (1995) 3807.

[17] SIMION 8.1.0.48-x32, (c) 2003-2012 Scientific Instrument Services, Inc. (SIS) http://www.sisweb.com; Primary author: David J. Manura, SIS (version 8.1/8.0/SL); SIMION 7.0 developed under Government Contract No. DE-AC07-99ID13727 at the Idaho National Laboratory (INL), Primary author: David A. Dahl, INL (version 7 and below); see also D.A. Dahl, T.R. McJunkin, J.R. Scott, *"Comparison of ion trajectories in vacuum and viscous environments using SIMION: Insights for instrument design"*, Int. J. Mass Spectrom. **266/1-3** (2007) 156-165.

[18] NIST Standard Ref. Database **71**, NIST Electron Inelastic-mean-free-path database version 1.1; by C. J. Powell and A. Jablonski (2000).

[19] G. Schiwietz, G. Xiao, P.L. Grande, E. Luderer, R. Pazirandeh, U. Stettner, *"Determination of the electron temperature in the thermal spike of amorphous carbon"*, Europhys. Lett. **47**, (1999) 384-390.

[20] R. Courths and S. Hüfner, *"Photoemission experiments on Copper"*, Phys. Rep. **112** (1984) 55-171.

[21] A. Föhlisch, O. Karis, M. Weinelt, J. Hasselström, A. Nilsson, and N. Mårtensson, *"Auger Resonant Raman Scattering in Itinerant Electron Systems: Continuum Excitation in Cu"*, Phys. Rev. Lett. **88** (2002) 027601

[22] G. Schiwietz, D.Kühn, K.Holldack, and N.Pontius (in preparation)